NANO LETTERS
Letter
Cite This: Nano Lett. 2019, 19, 3777−3781
pubs.acs.org/NanoLett

Room-Temperature Magnetic Order in Air-Stable Ultrathin Iron Oxide

Jiangtan Yuan,[†,⊥] Andrew Balk,[‡,⊥] Hua Guo,[†] Qiyi Fang,[†] Sahil Patel,[†] Xuanhan Zhao,[§] Tanguy Terlier,[∥] Douglas Natelson,[§] Scott Crooker,[‡] and Jun Lou*[,†]

[†]Department of Materials Science and NanoEngineering, Rice University, Houston, Texas 77005, United States
[‡]National High Magnetic Field Laboratory, Los Alamos, New Mexico 87545, United States
[§]Department of Physics and Astronomy, Rice University, Houston, Texas 77005, United States
[∥]Shared Equipment Authority, Rice University, Houston, Texas 77005, United States

Supporting Information

ABSTRACT: Manual assembly of atomically thin materials into heterostructures with desirable electronic properties is an approach that holds great promise. Despite the rapid expansion of the family of ultrathin materials, stackable and stable ferro/ferri magnets that are functional at room temperature are still out of reach. We report the growth of air-stable, transferable ultrathin iron oxide crystals that exhibit magnetic order at room temperature. These crystals require no passivation and can be prepared by scalable and cost-effective chemical vapor deposition. We demonstrate that the bonding between iron oxide and its growth substrate is van der Waals-like, enabling us to remove the crystals from their growth substrate and prepare iron oxide/graphene heterostructures.

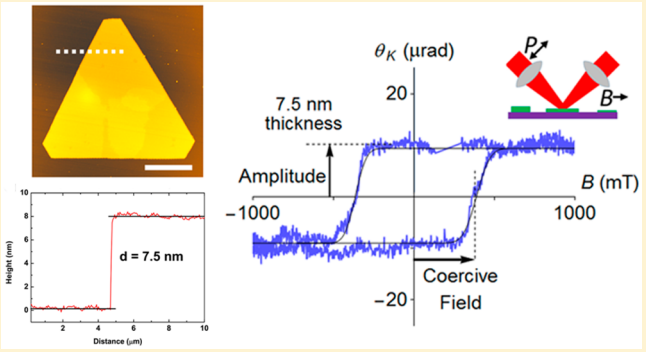

KEYWORDS: *Iron oxide, room-temperature magnetism, van der Waals heterostructure, ultrathin*

There is great interest in using mechanical stacking,[1,2] rather than epitaxial materials growth, to assemble heterostructures of materials which exhibit diverse, intriguing properties such as valley polarization,[3] ferroelectricity,[4] superconductivity,[5] and charge-density waves.[6,7] Efforts have been made to create stackable magnetic materials through engineering of defects, but only local magnetism has been achieved.[8−10] The recent discoveries of layered materials supporting intrinsic ferromagnetism have made stacked spintronic heterostructures realistic.[11−17] However, manual assembly of multilayer devices with these ferromagnets under ambient conditions remains challenging due to material sensitivity to environmental degradation, and magnetic order at room temperature is rare in van der Waals materials. Here, we show synthesis of ultrathin crystals of ε-Fe_2O_3 by scalable ambient pressure chemical vapor deposition (CVD), finding ready formation on both silicon dioxide and mica substrates. Electron microscopy and Raman spectroscopy measurements confirm that the crystals are pure ε-Fe_2O_3, with no detectable amounts of the more common α-Fe_2O_3 and γ-Fe_2O_3 phases, for crystals thinner than approximately 100 nm. Furthermore, the magneto-optical Kerr effect (MOKE) magnetometry of individual crystals shows that they are magnetically stable, with coercive fields of hundreds of mT. We observe robust hysteresis even in crystals as thin as 7 nm at room temperature in atmosphere. These samples of ultrathin ε-Fe_2O_3 can be readily transferred from growth substrates in aqueous solutions at ambient conditions to arbitrary substrates without any visible structural changes. Finally, despite the fact that these CVD-grown ultrathin ε-Fe_2O_3 crystals are not van der Waals materials, their atomically sharp surfaces and nanoscale thicknesses allow them to be easily integrated with two-dimensional (2D) materials such as graphene, thereby eliminating the lattice mismatching constraints for design of functional heterostructures. This CVD growth, manipulation, and magnetic study of comparatively large individual crystals is complementary to recent successes in liquid-phase exfoliation of ensembles of nanoscale ultrathin hematite crystals.[18]

ε-Fe_2O_3 has an orthorhombic structure with lattice constants a = 5.072 Å, b = 8.736 Å, c = 9.418 Å and belongs to the space group of $Pna2_1$.[19] There are four independent crystallographically nonequivalent iron sites, denoted as Fe_A, Fe_B, Fe_C, and Fe_D, occupying the center of either the octahedron or tetrahedron formed by surrounding oxygen atoms (Figure 1a). We grow samples with standard CVD techniques (see Methods for growth details in the SI). Ultrathin crystals of iron oxide with lateral size of ≈10 μm readily form using this procedure and are apparent in optical micrographs (Figure 1b−d). All crystals

Received: March 4, 2019
Revised: April 20, 2019
Published: May 6, 2019

DOI: 10.1021/acs.nanolett.9b00905
Nano Lett. 2019, 19, 3777−3781

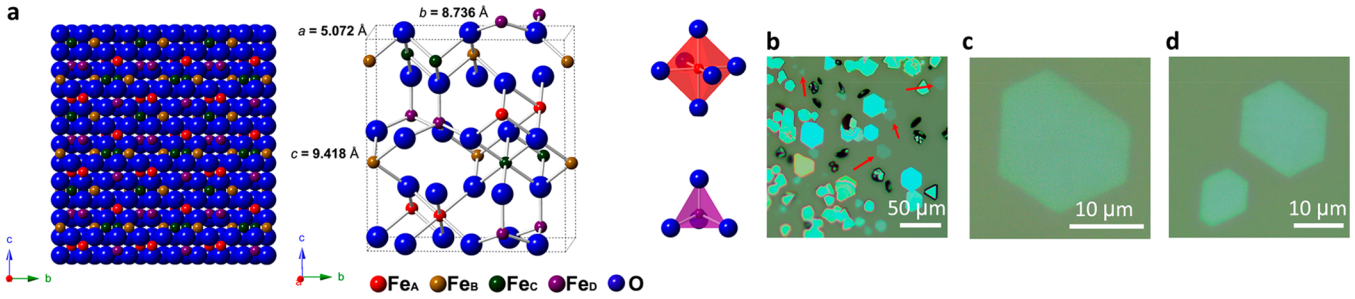

Figure 1. Crystal structure and optical images of ε-Fe_2O_3. (a) Nonlayered ε-Fe_2O_3 has an orthorhombic structure with a = 5.072 Å, b = 8.736 Å, and c = 9.418 Å. There are four independent iron sites, denoted as Fe_A, Fe_B, Fe_C, and Fe_D. Inset: Individual octahedron formed by one center iron atom and six surrounding oxygen atoms, representing the cation coordination of Fe_A, Fe_B, Fe_C, and an individual tetrahedron formed by one center iron atom and four surrounding oxygen atoms, representing the cation coordination of Fe_D. (b–d) Optical images of ε-Fe_2O_3 crystals grown on mica by CVD. Ultrathin crystals with a lateral size of many μm can be easily found in each batch of growth, as indicated by the red arrows. The out-of-plane growth direction is [001]. Grain structure of the crystals is discussed below.

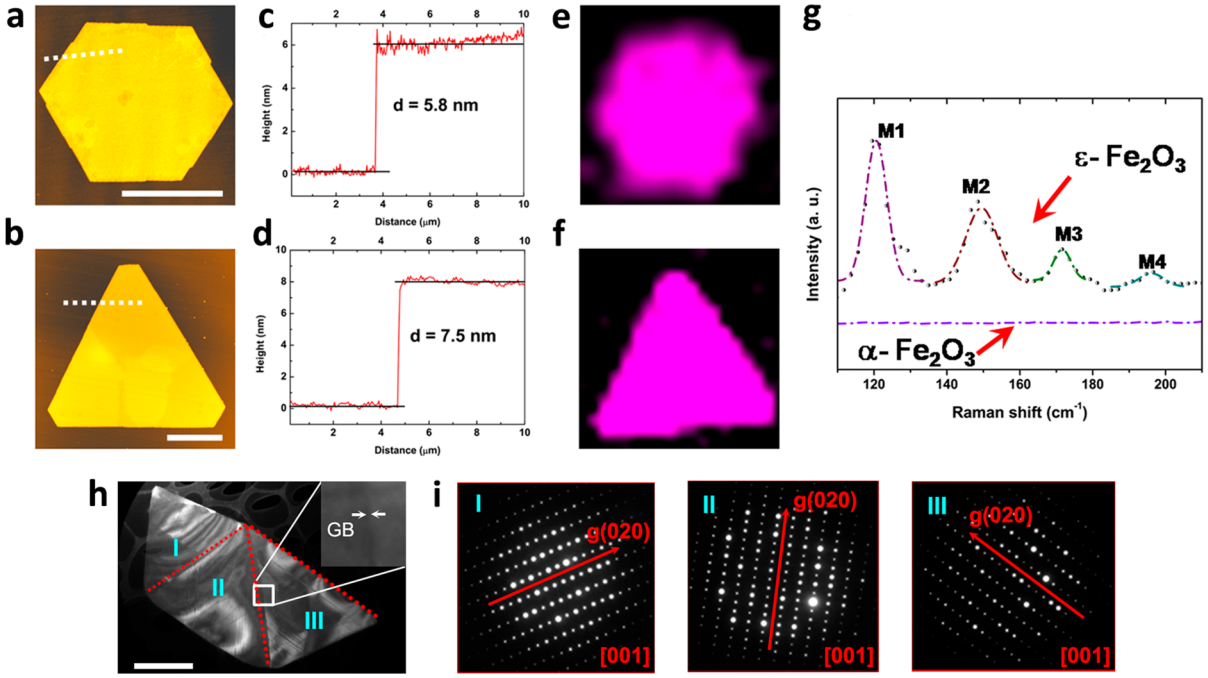

Figure 2. Characterization of ε-Fe_2O_3. (a, b) Two representative ultrathin ε-Fe_2O_3 crystals with hexagonal and triangular shapes grown on a mica substrate. The well-defined shapes indicate high crystal quality. Scale bars are 5 μm. (c, d) AFM thickness measurements for crystals in (a) and (b). The thicknesses are 5.8 and 7.5 nm, respectively. (e, f) The corresponding spatially resolved Raman mapping for crystals in (a) and (b). The intensities are the sum of signals between 100 and 200 cm^{-1}, normalized by the Raman peak of mica substrate. The homogeneous intensity distributions show that the ε-Fe_2O_3 phase is uniformly distributed within the crystals. (g) Raman spectra collected from ε-Fe_2O_3 and α-Fe_2O_3 crystals on silicon dioxide. The four characteristic peaks between 100 and 200 cm^{-1} represent the first-order phonon modes, namely M1–M4, of ε-Fe_2O_3, whereas α-Fe_2O_3 has no active Raman modes in this range. Peaks are fitted by Lorentz functions. (h) Dark-field TEM image of an ultrathin ε-Fe_2O_3 polycrystalline flake transferred from the mica substrate. At least three individual grains, marked by I, II, and III are present in this flake. GBs are highlighted by red dotted lines. Inset: Zoom-in image of a GB. (i) Electron diffraction patterns from three grains in (h), which can also be indexed to the orthorhombic symmetry of ε-Fe_2O_3 in the [001] zone axis. The angles between grains I and II and grains II and III are about 56° and 45°, respectively.

exhibit well-defined shapes with sharp edges, showing clear evidence of high crystallinity.

Figure 2a,b shows atomic force microscopy (AFM) images of two representative crystals with thicknesses of ≈5.8 nm and ≈7.5 nm (Figure 2c,d). The thinnest crystal we have measured is ≈5.1 nm, which is only five unit-cells thick. The ultrathin Fe_2O_3 crystals have atomically smooth surfaces and uniform thicknesses, with a standard deviation roughness <0.5 nm. Micro-Raman measurements of these samples (Figure 2g) show four peaks between 100 and 200 cm^{-1}, which are the characteristic first-order phonon vibration modes M1–M4 of ε-Fe_2O_3, in agreement with previous literature.[20] In comparison, the most stable bulk phase α-Fe_2O_3 has no Raman active modes in this range. Full spectrum comparison can be found in Figure S1. Spatially resolved Raman mappings (Figure 2e,f) further suggest uniformity within individual crystals. No detectable second phase was observed.

We employed transmission electron microscopy (TEM) to gain further structural insight of the as-synthesized ultrathin Fe_2O_3. Figure 2h is a dark-field TEM image of an ultrathin Fe_2O_3 polycrystalline flake where grain boundaries (GBs) can be visualized. The GBs are highlighted by red dotted lines, and

DOI: 10.1021/acs.nanolett.9b00905
Nano Lett. 2019, 19, 3777–3781

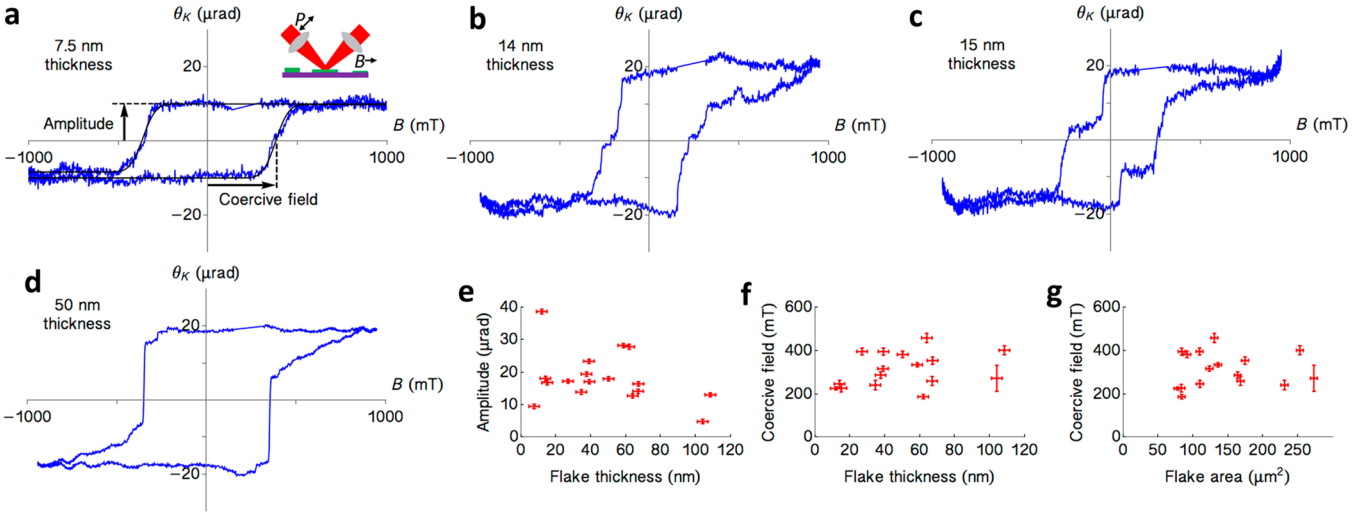

Figure 3. Room-temperature magnetic order in nanoscale thickness ε-Fe_2O_3. (a–d) MOKE hysteresis loops obtained from crystals with varying thicknesses from 7.5 to 50.1 nm, demonstrating magnetic order with symmetric hysteresis and coercive fields ≈300 mT. (e) The amplitude of the Kerr effect plotted against the thickness of the crystals measured by AFM, showing no correlation. (f) The coercive field plotted as a function of thickness, showing no obvious trend. Coercive fields and amplitudes are measured from the hysteresis loops by fitting the magnetic transitions to error functions. Backgrounds were removed from these hysteresis curves according to the procedure described in Figure S5. (g) The coercive field plotted as a function of flake area, showing no obvious trend.

a detail of a GB is displayed in the inset of Figure 2h. At least three grains, marked by I, II, and III, are present in this flake. The electron diffraction patterns (Figure 2i) from a randomly selected area in each grain can be indexed to the orthorhombic symmetry of ε-Fe_2O_3 in the [001] zone axis, consistent with the results from Raman spectroscopy (see SI Figure S2 for detailed phase index procedure). Although the three grains have the same out-of-plane growth direction, within the plane they orient differently, as indicated by the g (020) vectors. The angle between grains I and grain II is about 56° and between grains II and grain III is about 45°.

In addition to examining multiple randomly transferred crystals, we performed TEM and Raman analysis on the same thicker crystal (≈ 100 nm) by breaking it into two halves. The resulted TEM index matches well with that of Raman analysis (characteristic peaks between 100 and 200 cm^{-1}), confirming that Raman spectroscopy is an accurate and rapid way to identify ultrathin ε-Fe_2O_3. In total, we have checked 23 crystals with thicknesses ranging from 5.1 to 260 nm. Of these, 22 crystals show the ε phase (see SI Figure S3).

To provide more insights about the growth mechanism, we analyzed the ε-Fe_2O_3 flakes by time-of-flight secondary ion mass spectrometry (TOF-SIMS). The chemical mapping in Figure S4 reveals that the flakes are laterally uniform with a clear contrast between the flakes and mica substrate. A higher Cl signal in the flake regions (Figure S4b) indicates the preferential adsorption of Cl. In-depth analysis further confirms that Cl is present on the surface of the flake, while there is no noticeable Cl inside of the ε-Fe_2O_3 flake. This TOF-SIMS analysis provides evidence that the absorption of Cl might be one of the reasons why we can achieve highly anisotropic ultrathin growth for ε-Fe_2O_3.

We next probe the magnetic properties of these ultrathin ε-Fe_2O_3 crystals with longitudinal MOKE measurement at room temperature (295 K). The measurement geometry is shown in the inset of Figure 3a, and further details of the measurement and data processing are described in Methods. Figure 3a-d show typical hysteresis loops of Kerr rotation θ_K as a function of magnetic field, B, for samples with thickness ranging from 7.5 to 50.1 nm. These loops clearly show room-temperature magnetic order in ultrathin ε-Fe_2O_3 with well-defined transitions and coercive fields of hundreds of mT. Noting the difference in the amplitude of the Kerr effect, in particular between the 7.5 and 15 nm-thick samples (Figure 3a,c), we investigated 15 other crystals with different thicknesses to check for an influence of thickness on magnetic properties. Of these, all show a similar room temperature switching behavior, with a mean coercive field of 290 mT and a standard deviation of 80 mT. These results agree well with previous measurements of nanoparticles[21,22] and thin films of ε-Fe_2O_3.[23] To check the robustness of the magnetic properties of our samples at room temperature, we plot the coercive field and the amplitude of the magnetic transitions as a function of sample thickness, as measured by AFM. We find that neither the amplitude of the Kerr effect (Figure 3e) nor the coercive field (Figure 3f) correlates with sample thickness. This absence of correlation confirms the robustness of magnetic order of this material even in ultrathin thickness. This observation is in contrast with other magnetic samples. For example, magnetite (Fe_3O_4) films[24,25] and nanoparticles[26] show a strong dependence of coercive field on sample dimensions. In this regard, our data on ultrathin ε-Fe_2O_3 suggest that it has a promising potential in ultracompact information storage applications. We also plot the coercive field as a function of flake area in Figure 3g, which also shows no correlation. These observations suggest that the coercive field is set by local properties within the ε-Fe_2O_3, rather than by any thickness tuning of exchange processes or by geometric anisotropy.

Electronic transport measurements (see Figures S6 and S7) show that the material is highly resistive, with a room-temperature resistivity on the order of 100 Ω·m. This is comparable to expectations for the related oxide, hematite,[27,28] and implies high sample quality through the lack of doping from vacancies or impurities.

One distinctive advantage of ultrathin ε-Fe_2O_3 is that these crystals have exceptional stability. Figure 4a is an AFM image

DOI: 10.1021/acs.nanolett.9b00905
Nano Lett. 2019, 19, 3777–3781

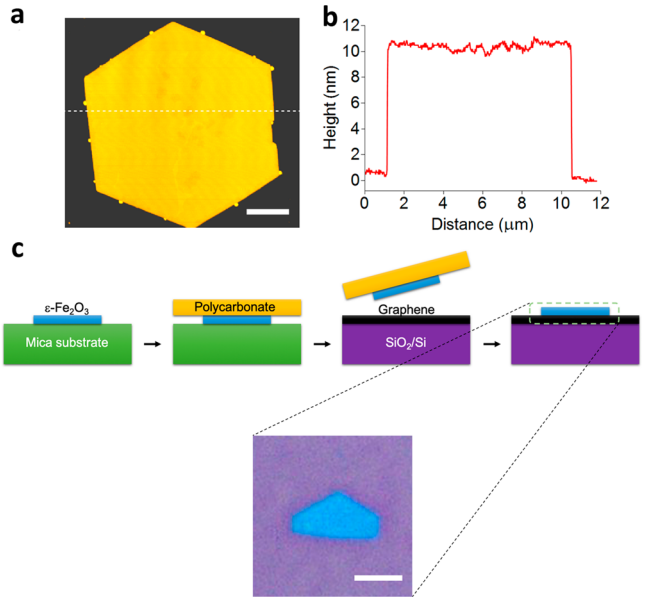

Figure 4. Stability and transferability of ultrathin ε-Fe_2O_3. (a) AFM image of a crystal stored under ambient conditions for over 3 months. No obvious voids or morphology changes can be observed. Scale bar: 2 μm. (b) Height profile analysis across the whole crystal indicates that the surface is highly smooth, with a standard deviation roughness of 0.28 nm, and edges are sharp without any signs of degradation. (c) Scheme of transferring ultrathin ε-Fe_2O_3 crystals from mica growth substrate and building an ε-Fe_2O_3/graphene heterostructure. The monolayer CVD-grown graphene film is on a SiO_2/Si substrate. Scale bar: 2 μm.

of a crystal stored in ambient condition (T = 24.0 °C, RH = 39%) for over 3 months. No obvious voids or morphology changes were observed. Height profile analyses across the whole sample (Figure 4b) reveals that the crystal still has an atomically smooth surface with a standard deviation roughness of 0.28 nm and sharp edges. Therefore, it is not likely that these ultrathin ε-Fe_2O_3 crystals will be further degraded, demonstrating extraordinary stability compared to other nanoscale magnetic materials reported so far. Remarkably, ultrathin ε-Fe_2O_3 can be transferred easily from the growth substrate like van der Waals layered materials. Taking advantage of its stability, we prepared a ε-Fe_2O_3/graphene film heterostructure through a water-assisted polycarbonate transfer method, where no harsh chemical etchants were involved. The transfer scheme and outcome are illustrated in Figure 4c. The well-defined and intact flake after transfer clearly demonstrates the bonding between ε-Fe_2O_3 and its growth substrate is noncovalent, thereby allowing ultrathin ε-Fe_2O_3 to be handled as a van der Waals material for building different types of heterostructure devices.

In summary, ultrathin ε-Fe_2O_3 can be synthesized via a scalable ambient CVD technique. MOKE measurements on individual crystals clearly show that ultrathin ε-Fe_2O_3 is magnetically ordered at room temperature with coercive fields of 200−400 mT and sharp magnetic transitions, even down to 7.5 nm thickness. Moreover, ultrathin ε-Fe_2O_3 will not degrade under ambient conditions for months. We further demonstrate that these crystals can be transferred from a growth substrate and integrated into a ε-Fe_2O_3/graphene heterostructure through well-established methods developed for 2D materials at ambient conditions. Thanks to these useful and unique properties, ultrathin ε-Fe_2O_3 will be a promising and distinctive platform to explore magnetism in the nanoscale limit. It is envisioned that new conceptual devices with novel spin functionalities could be developed through heterostructure engineering with other layered materials.

■ ASSOCIATED CONTENT

Supporting Information

The Supporting Information is available free of charge on the ACS Publications website at DOI: 10.1021/acs.nanolett.9b00905.

Materials and methods and Figures S1−S7 (PDF)

■ AUTHOR INFORMATION

Corresponding Author

*E-mail: jlou@rice.edu.

ORCID

Douglas Natelson: 0000-0003-2370-9859

Scott Crooker: 0000-0001-7553-4718

Jun Lou: 0000-0002-0200-3948

Author Contributions

⊥J.Y. and A.B. contributed equally. J.Y. and J.L. conceived the idea and designed the experiments. J.Y., S.P., and Q.F. conducted the materials growth and Raman and AFM characterization. A.B. and S.C. performed the MOKE measurements. A.B. processed and analyzed the MOKE data. H.G. carried out the TEM characterization and phase index from electron diffraction patterns. X.Z. and D.N. handled the device fabrication magnetotransport measurements. T.T. performed TOF-SIMS analysis. All authors wrote the manuscript and discussed the results at all stages. All authors have given approval to the final version of the manuscript.

Funding

The CVD growth, Raman, and AFM characterization of Fe_2O_3 was supported by the Welch Foundation (C-1716). TEM characterization was supported by a DOE BES grant (DE-SC0018193). MOKE measurements at the NHMFL were supported by the National Science Foundation DMR-1644779. Device fabrication and transport measurements were funded by Rice IDEA support and National Science Foundation DMR-1704264.

Notes

The authors declare no competing financial interest.

■ ACKNOWLEDGMENTS

We thank K. H. and L. Yang for their helpful discussion, C. Sui for assistance with TEM sample preparation, and P. Zhou for assistance with device fabrication. We acknowledge the support of the National Science Foundation for access to the TOF-SIMS at Rice University, supported through CBET1626418. TOF-SIMS analyses were carried out with support provided by the Shared Equipment Authority at Rice University.

■ REFERENCES

(1) Novoselov, K. S.; Mishchenko, A.; Carvalho, A.; Castro Neto, A. H. 2D materials and van der Waals heterostructures. *Science* **2016**, *353*, aac9439.

(2) Geim, A. K.; Grigorieva, I. V. Van der Waals heterostructures. *Nature* **2013**, *499*, 419−425.

(3) Mak, K. F.; McGill, K. L.; Park, J.; McEuen, P. L. The valley Hall effect in MoS_2 transistors. *Science* **2014**, *344*, 1489−1492.

(4) Chang, K.; Liu, J.; Lin, H.; Wang, N.; Zhao, K.; Zhang, A.; Jin, F.; Zhong, Y.; Hu, X.; Duan, W.; Zhang, Q.; Fu, L.; Xue, Q. K.; Chen,

DOI: 10.1021/acs.nanolett.9b00905
Nano Lett. 2019, 19, 3777−3781

X.; Ji, S. H. Discovery of robust in-plane ferroelectricity in atomic-thick SnTe. *Science* **2016**, *353*, 274−278.
(5) Gozar, A.; Logvenov, G.; Kourkoutis, L. F.; Bollinger, A. T.; Giannuzzi, L. A.; Muller, D. A.; Bozovic, I. High-temperature interface superconductivity between metallic and insulating copper oxides. *Nature* **2008**, *455*, 782−785.
(6) Xi, X.; Zhao, L.; Wang, Z.; Berger, H.; Forro, L.; Shan, J.; Mak, K. F. Strongly enhanced charge-density-wave order in monolayer $NbSe_2$. *Nat. Nanotechnol.* **2015**, *10*, 765−769.
(7) Ritschel, T.; Trinckauf, J.; Koepernik, K.; Buchner, B.; Zimmermann, M. v.; Berger, H.; Joe, Y. I.; Abbamonte, P.; Geck, J. Orbital textures and charge density waves in transition metal dichalcogenides. *Nat. Phys.* **2015**, *11*, 328−331.
(8) Magda, G. Z.; Jin, X.; Hagymasi, I.; Vancso, P.; Osvath, Z.; Nemes-Incze, P.; Hwang, C.; Biro, L. P.; Tapaszto, L. Room-temperature magnetic order on zigzag edges of narrow graphene nanoribbons. *Nature* **2014**, *514*, 608−611.
(9) Gonzalez-Herrero, H.; Gomez-Rodriguez, J. M.; Mallet, P.; Moaied, M.; Palacios, J. J.; Salgado, C.; Ugeda, M. M.; Veuillen, J.-Y.; Yndurain, F.; Brihuega, I. Atomic-scale control of graphene magnetism by using hydrogen atoms. *Science* **2016**, *352*, 437−441.
(10) Seixas, L.; Carvalho, A.; Castro Neto, A. H. Atomically thin dilute magnetism in Co-doped phosphorene. *Phys. Rev. B: Condens. Matter Mater. Phys.* **2015**, *91*, 155138.
(11) Huang, B.; Clark, G.; Navarro-Moratalla, E.; Klein, D. R.; Cheng, R.; Seyler, K. L.; Zhong, D.; Schmidgall, E.; Mcguire, M. A.; Cobden, D. H.; Yao, W.; Xiao, D.; Jarillo-Herrero, P.; Xu, X. Layer-dependent ferromagnetism in a van der Waals crystal down to the monolayer limit. *Nature* **2017**, *546*, 270−273.
(12) Gong, C.; Li, L.; Li, Z.; Ji, H.; Stern, A.; Xia, Y.; Cao, T.; Bao, W.; Wang, C.; Wang, Y.; Qiu, Z. Q.; Cava, R. J.; Louie, S. G.; Xia, J.; Zhang, X. Discovery of intrinsic ferromagnetism in two-dimensional van der Waals crystals. *Nature* **2017**, *546*, 265−269.
(13) Bonilla, M.; Kolekar, S.; Ma, Y.; Diaz, H. C.; Kalappattil, V.; Das, R.; Eggers, T.; Gutierrez, H. R.; Phan, M.-H.; Batzill, M. Strong room-temperature ferromagnetism in VSe_2 monolayers on van der Waals substrates. *Nat. Nanotechnol.* **2018**, *13*, 289−293.
(14) Song, T.; Cai, X.; Tu, M. W.-Y.; Zhang, X.; Huang, B.; Wilson, N. P.; Seyler, K. L.; Zhu, L.; Taniguchi, T.; Watanabe, K.; McGuire, M. A.; Cobden, D. H.; Xiao, D.; Yao, W.; Xu, X. Giant tunneling magnetoresistance in spin-filter van der Waals heterostructures. *Science* **2018**, *360*, 1214−1218.
(15) Klein, D. R.; MacNeill, D.; Lado, J. L.; Soriano, D.; Navarro-Moratalla, E.; Watanabe, K.; Taniguchi, T.; Manni, S.; Canfield, P.; Fernandez-Rossier, J.; Jarillo-Herrero, P. Probing magnetism in 2D van der Waals crystalline insulators via electron tunneling. *Science* **2018**, *360*, 1218−1222.
(16) Deng, Y.; Yu, Y.; Song, Y.; Zhang, J.; Wang, N. Z.; Sun, Z.; Yi, Y.; Wu, Y. Z.; Wu, S.; Zhu, J.; Wang, J.; Chen, X. H.; Zhang, Y. Gate-tunable room-temperature ferromagnetism in two-dimensional Fe_3GeTe_2. *Nature* **2018**, *563*, 94−99.
(17) Fei, Z.; Huang, B.; Malinowski, P.; Wang, W.; Song, T.; Sanchez, J.; Yao, W.; Xiao, D.; Zhu, X.; May, A. F.; Wu, W.; Cobden, D. H.; Chu, J.-H.; Xu, X. Two-dimensional itinerant ferromagnetism in atomically thin Fe_3GeTe_2. *Nat. Mater.* **2018**, *17*, 778−782.
(18) Puthirath Balan, A.; Radhakrishnan, S.; Woellner, C. F.; Sinha, S. K.; Deng, L.; Reyes, C.; Rao, B. M.; Paulose, M.; Neupane, R.; Apte, A.; Kochat, V.; Vajtai, R.; Harutyunyan, A. R.; Chu, C.-W.; Costin, G.; Galvao, D. S.; Marti, A. A.; van Aken, P. A.; Varghese, O. K.; Tiwary, C. S.; Ramaswamy Iyer, A.; Ajayan, P. M. Exfoliation of a non-van der Waals material from iron ore hematite. *Nat. Nanotechnol.* **2018**, *13*, 602−609.
(19) Tucek, J.; Zboril, R.; Namai, A.; Ohkoshi, S. Epsilon-Fe_2O_3: an advanced nanomaterial exhibiting giant coercive field, millimeter-wave ferromagnetic resonance, and magnetoelectric coupling. *Chem. Mater.* **2010**, *22*, 6483−6505.
(20) Lopez-Sanchez, J.; Serrano, A.; Del Campo, A.; Abuin, M.; Rodriguez de la Fuente, O.; Carmona, N. Sol-gel synthesis and micro-Raman characterization of epsilon-Fe_2O_3 micro- and nanoparticles. *Chem. Mater.* **2016**, *28*, 511−518.
(21) Jin, J.; Ohkoshi, S.; Hashimoto, K. Giant coercive field of nanometer-sized iron oxide. *Adv. Mater.* **2004**, *16*, 48−51.
(22) Taboada, E.; Gich, M.; Roig, A. Nanospheres of silica with an epsilon-Fe_2O_3 single crystal nucleus. *ACS Nano* **2009**, *3*, 3377−3382.
(23) Gich, M.; Gazquez, J.; Roig, A.; Crespi, A.; Fontcuberta, J.; Idrobo, J. C.; Pennycook, S. J.; Varela, M.; Skumryev, V.; Varela, M. Epitaxial stabilization of epsilon-Fe_2O_3 (00l) thin films on $SrTiO_3$ (111). *Appl. Phys. Lett.* **2010**, *96*, 112508.
(24) Moussy, J.-B.; Gota, S.; Bataille, A.; Guittet, M.-J.; Gautier-Soyer, M.; Delille, F.; Dieny, B.; Ott, F.; Doan, T. D.; Warin, P.; Bayle-Guillemaud, P.; Gatel, C.; Snoeck, E. Thickness dependence of anomalous magnetic behavior in epitaxial Fe_3O_4(111) thin films: Effect of density of antiphase boundaries. *Phys. Rev. B: Condens. Matter Mater. Phys.* **2004**, *70*, 174448.
(25) Margulies, D. T.; Parker, F. T.; Spada, F. E.; Goldman, R. S.; Li, J.; Sinclair, R.; Berkowitz, A. E. Anomalous moment and anisotropy behavior in Fe_3O_4 films. *Phys. Rev. B: Condens. Matter Mater. Phys.* **1996**, *53*, 9175−9187.
(26) Goya, G. F.; Berquo, T. S.; Fonseca, F. C.; Morales, M. P. Static and dynamic magnetic properties of spherical magnetite nanoparticles. *J. Appl. Phys.* **2003**, *94*, 3520−3528.
(27) Morin, F. J. Electrical properties of α-Fe_2O_3 and α-Fe_2O_3 containing titanium. *Phys. Rev.* **1951**, *83*, 1005.
(28) Glasscock, J. A.; Barnes, P. R. F.; Plumb, I. C.; Bendavid, A.; Martin, P. J. Structural, optical and electrical properties of undoped polycrystalline hematite thin films produced using filtered arc deposition. *Thin Solid Films* **2008**, *516*, 1716−1724.

DOI: 10.1021/acs.nanolett.9b00905
Nano Lett. 2019, 19, 3777−3781